SMALL ANGLE X-RAY SCATTERING STUDIES OF CARBON ANODES USED IN LITHIUM RECHARGEABLE BATTERIES

[†]Giselle Sandí*, [†]Kathleen A. Carrado, [†]Randall E. Winans,
[†]Sönke Seifert, and [††]Christopher S. Johnson

Argonne National Laboratory, [†]Chemistry and [††]Chemical Technology Divisions,
9700 South Cass Ave., Argonne, IL 60439

ABSTRACT

In our laboratories, disordered carbons with predictable surface area and porosity properties have been prepared using inorganic templates containing well-defined pore sizes. The carbons have been tested in electrochemical cells as anodes in lithium secondary batteries. They deliver high specific capacity and display excellent performance in terms of the number of cycles run. *In situ* small angle X-ray scattering (SAXS) during electrochemical cycling was carried out at the Advanced Photon Source, at ANL. In order to monitor the carbon electrode structural changes upon cycling, an electrochemical cell was specially designed to allow for the application of electrical current and the collection of SAXS data at the same time. Results show that upon cycling the structure of the carbon remains unchanged, which is desirable in reversible systems. The fractal dimension and the invariant do not show significant variation upon cycling the templated carbon electrode. However, large variations were observed for the graphite electrode, indicating changes in the sample topology.

KEYWORDS: SAXS, carbon anodes, lithium secondary batteries

INTRODUCTION

Carbonaceous materials have received considerable interest for use as anodes ever since Sony introduced the lithium-ion battery [1,2]. Carbon containing systems are noted for potential safety and reliability advantages because the carbon anodes are less prone to form dendrites than metallic lithium anodes. Most investigations have utilized carbon materials that are available from existing sources such as natural graphite, cokes, carbon fibers, non-graphitizable carbon, and pyrolitic carbon [3,4]. In these studies, high lithium capacities have been found to be associated with either disorder [5] or the presence of hydrogen [6].

An alternative avenue is the custom synthesis of carbons specifically tailored for use as anodes in lithium-ion batteries. This latter approach provides predictable control over critical properties such as the surface area and the porosity. Previously, Sandí and coworkers employed pillared clays with known interplanar spacing as templates for the synthesis of custom carbon anode materials [7-9]. They have also recently found that carbons with curved lattices can exhibit enhanced lithium capacity over that of graphite [10].

Our latest approach focuses on the use of sepiolite clay to tailor the synthesis of carbonaceous materials. Sepiolite is a phyllosilicate clay insofar as it contains a continuous two-dimensional tetrahedral silicate sheet. However, it differs from other clays in that it lacks a continuous octahedral sheet structure. Instead, its structure can be considered to contain ribbons of 2:1 phyllosilicate structure, with each ribbon linked to the next by inversion of SiO_4 tetrahedra along a set of Si-O-Si bonds. In this framework, rectangular channels run parallel to the x-axis between opposing 2:1 ribbons, which results in a fibrous morphology with channels running parallel to the fiber length. Channels are 3.7 x 10.6 Å in sepiolite (they are 3.7 x 6.4 Å in palygorskite). Individual fibers generally range from about 100 Å to 4-5 microns in length, 100-300 Å width, and 50-100 Å thickness. Inside the channels are protons, coordinated water, a small number of exchangeable cations, and zeolitic water. There are three sorption sites in sepiolite: (a) oxygen ions on the tetrahedral sheets, (b) a small amount of cation exchange sites (0.1-0.15 meq/100gm), and (c) SiOH groups along the fiber axis. Adsorption is also influenced by the size, shape, and polarity of

the molecules involved. The SiOH groups act as neutral adsorption sites suitable for organic species. These factors are all important to our goal of loading the clay with certain organic monomers that will polymerize on the surface and, following a pyrolysis step, carbonize to a material suitable for use as a carbonaceous anode in secondary lithium batteries.

Our main objective is to synthesize carbon with pores sizes capable of Li^+ diffusion in a rechargeable battery. The carbonaceous materials are derived from ethylene or propylene upon incorporation in the vapor phase in the channels of sepiolite, taking advantage of the Brønsted acidity in the channels to polymerize olefins. In order to monitor the carbon electrode structural changes upon cycling, an electrochemical cell was specially designed to allow for the application of electrical current and the collection of SAXS data at the same time.

EXPERIMENTAL

Details about the synthesis of the carbonaceous materials can be found in reference [11]. In summary, ethylene and propylene (AGA, 99.95%) were loaded and pyrolyzed in the gas phase in one step. A three-zone furnace was used. Quartz boats containing sepiolite were placed within a quartz tube. The temperature of the oven was gradually increased from room temperature (about 5 °C/min) to 700 °C. The oven was then held at that target temperature for 4 hours. The clay from the loaded/pyrolyzed sepiolite sample was removed using HF. It was then rinsed to neutral pH and refluxed with concentrated HCl for 2 hours. The sample was washed with distilled water until the pH was > 5 to ensure that there was no acid left. The resultant carbon was oven dried overnight at 120 °C.

In situ small angle X-ray scattering (SAXS) during electrochemical cycling was carried out at the Advanced Photon Source, (Basic Energy Sciences Synchrotron Research Center CAT), Argonne National Laboratory. Monochromatic X-rays (8.8 keV), are scattered off the sample and collected on a 18 x 18 cm^2 position sensitive two-dimensional gas detector. The scattered intensity has been corrected for absorption and instrument background. The intensity has been expressed as a function of the scattering vector Q, which is defined as: $Q = (4\pi/\lambda)\sin\theta$, where λ is the wavelength of the X-rays and θ is the scattering half angle. The value of Q is proportional to the inverse of the length scale ($Å^{-1}$). The instrument was operated with a sample-to-detector distance of 68.5 cm to obtain data at $0.04 < Q < 0.7$ $Å^{-1}$. For these studies, a specially designed sample cell was used to record both the electrochemical response and SAXS data at the same time (see figure 1). The carbon sample was mixed with a teflon binder suspension (80/20 % w/w). The sample was oven dried and pressed against a Cu mesh. The electrode was then dried out in a vacuum oven at 80°C overnight. A piece of lithium foil (0.008"; 0.203 mm from FMC Lithium Division, Gastonia, NC) with the same dimensions as the carbon composite was also pressed against Cu mesh. A propylene membrane (Hoechst-Celanese, Charlotte NC) was used as the separator. The electrodes were held together by using kapton tape along the edges. The electrolyte was 1 M $LiPF_6$ in a mixture of 50% v/v ethylcarbonate and 50 % v/v diethylcarbonate (Merck, Germany). A control experiment was performed using commercial graphite (Aldrich). The cell was discharged from the open circuit voltage (OCV) to 0 V and back to 2.5 V at a scan rate of 0.1 mV/s using a EG&G 273A potentiostat.

RESULTS AND DISCUSSION

In order to monitor the carbon electrode structural changes upon cycling, an electrochemical cell was specially designed to allow for the application of electrical current and the collection of SAXS data at the same time. The availability of very intense X-rays from synchrotron sources enables the use of SAXS to study the meso and micropore size distributions of many materials. Small-angle scattering from x-rays arises due to the presence of discontinuities in the density of a material. Thus, the particles and pores in the carbons can produce strong small angle scattering signals in a wide momentum-transfer range. The small angle scattering data can be modeled to obtain information on the microstructure of the porous network. In battery applications, if the liquid organic electrolyte penetrates the pores of the carbon anode, it leads to irreversible electrolyte decomposition during the first

electrochemical reaction of lithium with the carbon, and hence a large irreversible capacity. If the pores are small (of the order of 15 Å or less), and the structure remains intact, the liquid electrolyte cannot penetrate, so excellent reversible behavior should be expected.

Figure 2 shows a typical two-dimensional plot of the time-resolved studies of a lithium ion cell made with carbon derived from sepiolite/propylene composite (upper curves) and an electrode made from commercial graphite (bottom curves). A spectrum was taken of the cell at the open circuit voltage (OCV = 2.99 V for the templated carbon and 2.70 V for the graphite electrode) and used as the background correction for the subsequent measurements. Upon application of voltage, a spectrum was taken every 60 mV (every 5 minutes). The results obtained for the templated carbon indicated that during cycling, there are no structural changes upon lithium intercalation as is evidenced by the near overlap of all curves. This means that solvent penetration into the carbon anode, which causes irreversible capacity, is avoided and so excellent reversibility is attained. The results of the control experiment using commercial graphite clearly indicates that there are changes in the structure of graphite and that these changes are not reversible.

These curves can be analyzed to determine size of features, topology, and changes in total scattering. At small Q in the Guinier region, the radius of gyration (Rg), which is related to the size of the scattering features, can be determined. For example, Rg for spheres can be determined from the slope of I(Q) vs Q^2 in a Q region where Rg Q < 1.0. Power law slope (fractal dimension) from the data is used to describe the topology of the system. Figure 3 shows the variation of the power law as a function of the applied voltage for both systems. For a layered material such a graphite a fractal dimension close to 2 is typical. When there is no lithium in the graphite lattice (at the OCV voltage), the fractal dimension must be close to the original material. In this case, the fractal dimension corresponded to 2.028, in excellent agreement to the theoretical value. As the voltage decreases, large fluctuations in the power law as a function of voltage are observed. At about 1.2 V, where the intercalation of lithium begins, the value of the power law increases to 2.16, indicating that the layers are expanding. These changes, however, are not reversible since the lattice does not contract to the original position. This is not the case for the templated carbon electrode, where the fractal dimension remains fairly constant throughout the voltage range. Since this is a disordered carbon, it is expected that the power law would be higher than graphite. The initial value corresponded to 2.57 and there are no significant changes throughout the measurement.

The invariant, Q_0, is proportional to the square of the electron density difference in the system, and is calculated as follows:

$$Q_0 = \int_0^\infty I(Q)\, Q^2\, dQ$$

Figure 4 shows a plot of invariant as a function of voltage for both electrodes. As expected, large variations in the electron density occur in the graphite electrode (especially at > 1.2 V) probably due to solvent incorporation upon irreversible lattice expansion, whereas the templated carbon shows variation within the statistical error.

CONCLUSIONS

Based on the electrochemical performance and much higher structural stability compared to graphite, carbon anodes derived from sepiolite as templates are demonstrated as good candidates for lithium ion cells. The synthetic approach described here yielded well defined carbon tubes with little or no graphitic character as evidenced by TEM. The yield of carbon based on the amount of inorganic template is about 25 times higher than our previous synthetic method, which makes it viable for commercial applications.

ACKNOWLEDGMENTS

This work has benefit from the use of the Advance Photon Source at Argonne National Laboratory, and was performed under the auspices of the U.S. Department of Energy, Office of Basic Energy Sciences, Division of Chemical Sciences, under contract number W-31-109-ENG-38.

REFERENCES

[1] D. Linden (ed.), *Handbook of Batteries*, 2nd edition, p.36, McGraw Hill, New York (1995).
[2] T. Nagaura and K. Tozawa, *Progress in Batteries and Solar Cells*, **9**, 209 (1990).
[3] R. Takagi, T. Okubo, K. Sekine, and T. Takamura, *Denki Kagaku*, **65**, 333 (1997).
[4] H. H. Schönfelder, K. Kitoh, and H. Nemoto, *J. Power Sources*, **68**, 258 (1997).
[5] Y. Liu, J. S. Xue, T. Zheng, and J. R. Dahn, *Carbon*, **33**, 193 (1996).
[6] P. Papanek, M. Radosavljevic, and J. Fischer, *Chem. Mater.*, **8**, 1519 (1996).
[7] G. Sandí, R. E. Winans, and K. A. Carrado, *J. Electrochem. Soc.*, **143**, L95 (1996).
[8] G. Sandí, K. A. Carrado, R. E. Winans, J. R. Brenner, and G. W. Zajac, *Mater. Res. Soc. Symp. Proc., Macroporous and Microporous Materials*, **431**, 39 (1996).
[9] G. Sandí, R. E. Winans, K. A. Carrado, C. S. Johnson, and P. Thiyagarajan, *J. New Mat. Electrochem. Systems*, **1**, 83 (1998).
[10] L. G. Scanlon and G. Sandí, *Journal of Power Sources* **81-82**, 176 (1999).
[11] G. Sandí, K. A. Carrado, R. E. Winans, C. S. Johnson, and R. Csencsits, *J. Electrochem. Soc.*, **146**, 3644 (1999).

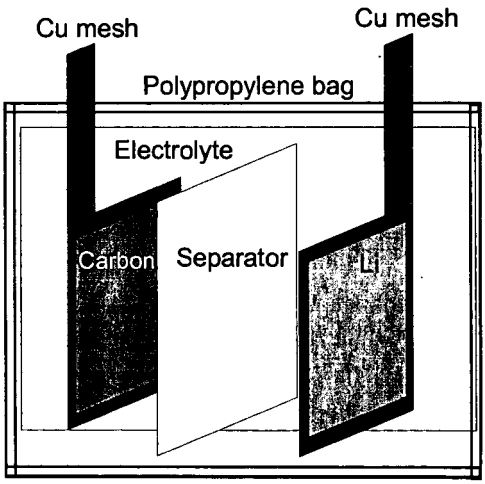

Figure 1: SAXS electrochemical cell for in situ measurements.

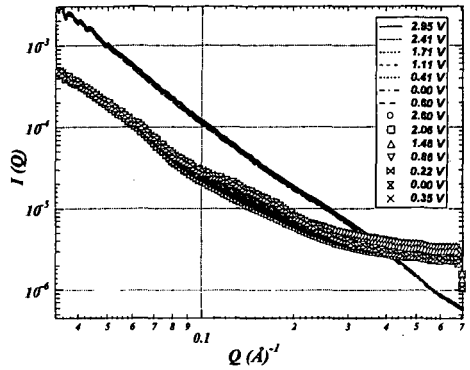

Figure 2: SAXS of electrodes made with templated carbon (upper lines) and commercial graphite (bottom symbols).

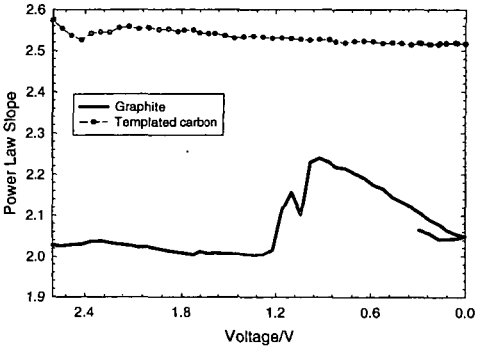

Figure 3: Variation of the power law as a function of discharged voltage of graphite and template electrodes.

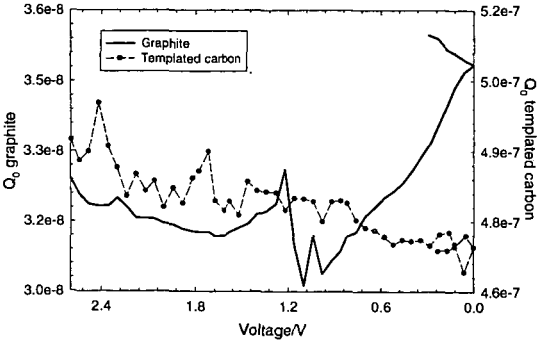

Figure 4: Invariant fluctuations as a function of discharge voltage of graphite and template electrodes.

STIMULI-RESPONSIVE POLYMER-GRAFTED LIPID-BASED COMPLEX FLUIDS AS ORGANIZED MEDIA FOR SUPRAMOLECULAR PHOTOCHEMISTRY

M.A. Firestone [1], D. M. Tiede [1], S. Seifert [1], and P. Thiyagarajan[2]
[1]Chemistry and [2]Intense Pulsed Neutron Source Division,
Argonne National Laboratory, Argonne, IL 60439

Keywords: Complex-Fluids, Stimuli-Responsive, Photochemistry

INTRODUCTION

Recent studies involving the use of micelles, reverse micelles, and microemulsions as organized microheterogeneous media for effecting photochemical transformations have led to growing recognition that the nature of the reaction medium (*i.e.*, microenvironment) may strongly influence the course and efficiency of photoinduced electron transfer (1,2). Of particular interest in photochemical energy conversion research is the study of such effects in natural photosynthesis, the process whereby plants and photosynthetic bacteria convert light into chemical energy. The primary process in photosynthesis occurs in transmembrane pigment-protein complexes called reaction centers (RCs), where following the absorption of light, primary charge separation occurs. This electrochemical energy is stored, and the initial charge separation used to drive all subsequent electron and proton transfer reactions in photosynthesis.

The bacterial photosynthetic reaction center provides an excellent protein-pigment complex with which to explore the influence of environment on biological electron transfer, as it is a membrane-associated protein that has been structurally well-characterized and that can be readily isolated from natural photosynthetic membranes and purified (3). One area of current research interest is the determination of the effect of conformational changes in detergent-solubilized RCs on electron transfer (4). In this report, we consider a related issue: the introduction of RCs into biomembrane mimetics and its impact on protein conformation, orientation, and function. As a medium for these studies, we have employed a recently developed a stimulus-responsive complex fluid (smart material) that possesses the ability to respond to an environmental change/external stimulus on a molecular level and amplify it in the form of a macroscopically observable phase/structural change (5). Specifically, this material undergoes a dramatic, thermoreversible phase change from a fluid, micellar phase to a biomembrane-mimetic, lamellar gel phase as the temperature is raised above 16°C. Macroscopically, this phase change manifests itself as a change from a low-viscosity state with no detectable optical birefringence to a high-viscosity (gel) state that shows strong birefringence (i.e., liquid crystal). This complex fluid comprises three organic solids: a zwitterionic surfactant, a phospholipid, and a PEGylated phospholipid that spontaneously self-assembles into a non-covalent aggregate when dispersed in water. The inverted phase behavior (*i.e.*, a fluid phase at a lower temperature than the liquid-crystalline gel phase) of this composition is unique, and allows delicate biological macromolecules (*e.g.*, membrane proteins) to be introduced/dispersed in the complex fluid at low temperature and transferred to the ordered, liquid-crystalline phase by simply warming to room temperature. This material thus offers new opportunities for conducting studies of supramolecular photochemistry, for performing fundamental investigations on proteins such as RCs in native-like environments, and for examining how protein functioning is modulated by the surrounding medium. In addition, this complex fluid offers the potential for harnessing the native functioning of biological molecules for the development of protein-based devices for electro-optic and/or solar energy conversion by spatially organizing them in a synthetic matrix.

EXPERIMENTAL

Preparation of Reaction Centers and Complex Fluids. Membrane-associated, photosynthetic reaction centers (RCs) from the photosynthetic bacterium *Rhodobacter sphaeroides* R-26 were isolated and purifed using established procedures (6). Briefly, the RCs were extracted from chromatophores with a solution consisting of 0.6% (w/v) LDAO, 100 mM NaCl, and 10 mM Tris at pH 7.8, and partially purified by ammonium sulfate fractionation followed by sucrose density gradient centrifugation. Final purification was achieved on a DEAE Sephracel column by extensive washing with a solution of 0.06% (w/v) LDAO, 60 mM NaCl, and 10mM Tris at pH 7.8. Purified RCs were eluted from the column with 0.06% (w/v) LDAO, 280 mM NaCl, 10 mM Tris pH 7.8. RCs were dialyzed against 100 mM NaCl, 10 mM Tris pH 7.8, 0.1% LDAO prior to introduction into the complex fluid. The complex fluid was prepared by hydration of the organic components, dimyristoylphosphatidylcholine (DMPC), 1,2-dimyristoyl-*sn*-glycero-3-phosphoethanolamine-N-poly(ethylene glycol) (DMPE-EO_{45}), and lauryldimethylamine-N-oxide (LDAO) using the composition reported previously (5).

Physical Methods. UV-visible-NIR absorption spectra were recorded using a Shimadzu 1601 spectrophotometer at a spectral resolution of 2 nm. Time-resolved spectroscopic measurements were made with a single-beam, pump-probe, diode array instrument following procedures previously

described (7). Synchrotron small angle X-ray scattering (SAXS) measurements were preformed either on the BESSRC undulator beamline (12ID) of the Advanced Photon Source (APS) at Argonne National Laboratory or at the Stanford Synchrotron Radiation Laboratory (SSRL, Stanford, CA) on beamline 4-2. The scattering profiles were recorded at APS were made with a mosaic detector composed of 9 CCD chips with an imaging area of 15 x 15 cm, with 1536 x 1536 pixel resolution. The scattering curves collected at SSRL recorded using a linear detector (BioLogic, Grenoble, France). The sample-to-detector distances were set such that the detecting range for momentum transfer was $0.006 < Q < 0.3$ Å^{-1} at SSRL and $0.008 < Q < 0.8$ Å^{-1} at APS. Samples were held in 1.5 mm quartz capillaries or in 1mm pathlength plexiglass cells with quartz coverslips as windows. Data were corrected for background scattering and calibrated based upon the known positions of silver behenate powder Bragg reflections. Small angle neutron scattering was performed on the SAND beamline at the Intense Pulsed Neutron Source (IPNS), at Argonne National Laboratory. The average wavelength of radiation was 1-14 Å and the momentum transfer, Q was 0.0035 - 0.6 Å. Samples were held in sealed, 1mm pathlength quartz cells. Sample temperature was regulated by a water recirculating bath and measured using a calibrated thermocouple. Low temperature measurements were carried out with the sample chamber under a N_2 atmosphere. Samples were prepared with D_2O, thereby eliminating the large incoherent background arising from H_2O and enhancing the contrast between the lipid aggregates and the solvent. Data were collected with the sample-to-detector distance of 1.54 m. Scattered neutrons were measured using a 128 x 128 array of position-sensitive, gas-filled 40 x 40 cm proportional counters, while the wavelengths were measured by time-of-flight. Data were collected for 5-8 h and reduced using standard methods (9).

RESULTS AND DISCUSSION

In our initial investigations, the effect of introducing RCs into the stimuli-responsive complex fluid on the extent of denaturation of the protein and its functional properties were examined. Introduction of the protein (as a solution in its detergent-solubilized state) into the preformed complex fluid produced an optically transparent, deep blue gel at room temperature. Evaluation of the extent of retention of the native structure and photochemical activity of the reconstituted RCs was carried out by two spectroscopic assays. First, the stability of reaction centers within the gel phase of the complex fluid was determined by monitoring the position and relative intensities of the co-factor absorption bands. The photosynthetic reaction center from *Rhodobacter sphaeroides* R26 is a large protein (10^5 kD) composed of three protein subunits (L, M, H) encasing nine co-factors arranged in *ca.* C_2 symmetry (3) (Figure 1B, C). Two bacteriochlorophyll molecules comprise the special pair that functions as the primary electron donor. On each side of this dimer is a bacteriochlorophyll monomer (Bchl) that, in turn, lies adjacent to a bacteriopheophytin (Bph), followed by a ubiquinone. A non-heme iron separates the primary quinone (Qa) from the terminal acceptor, the secondary quinone (Qb). The room temperature, ground-state absorption spectrum of the reaction center in the near-IR region shows three major absorbance bands, the position and intensities of which are sensitive to the integrity of the co-factors and local protein environment.

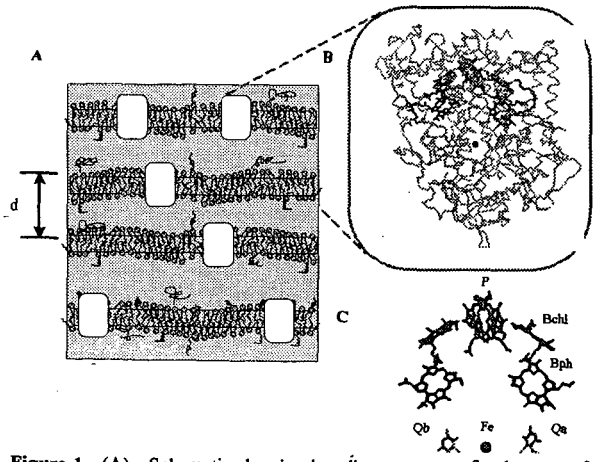

Figure 1. (A). Schematic showing lamellar structure of polymer-grafted lipid-based complex fluid with possible arrangement of reconstituted RCs. (B). The molecular structure of the photosynthetic reaction center (RC) of purple bacteria (*Rhodobacter sphaeroides* R26). (C). Co-factor arrangement of RCs taken from X-ray crystal structure data (3).

These absorption peaks, whose intensities are *ca.* 1:2:1, arise from the bacteriopheophytin (Bph, 755 nm), monomeric bacteriochlorophyll (Bchl, 802 nm), and bacteriochlorophyll dimer (P, 865 nm) cofactors. A comparison of the NIR absorption spectra of reaction centers in their detergent solubilized state and after their reconstitution into the lamellar gel phase of the complex fluid is presented in Figure 2. The close correspondence between the two spectra demonstrates that reaction centers can be successfully incorporated into the complex fluid without loss of structural integrity.

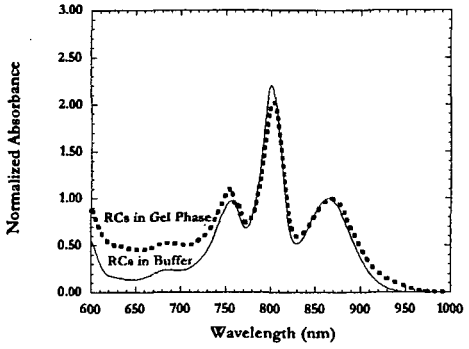

Figure 2. NIR absorption spectra of RCs in 10mM Tris-100mM NaCl-0.01%LDAO-0.01mM EDTA-pH7.8 buffer solution (solid line) and in polymer-grafted membrane-mimetic gel (dashed line).

The second spectroscopic assay involved evaluation of the photosynthetic activity of the RC in the gel phase of the complex fluid. A well-documented, diagnostic assay for reaction center photochemistry is the measurement of the laser flash-induced, transient absorbance decrease and recovery of the 865 nm absorption band of the primary electron donor chlorophyll, P (7). That is, following laser-induced, ps charge separation, the photosynthetic reaction ends with electron transfer between quinone cofactors (accompanied by proton uptake), Q_A and Q_B:

$$PQ_AQ_B + h\nu \rightleftharpoons P^+Q_A^-Q_B \rightleftharpoons P^+Q_AQ_B^-.$$

This electron transfer (between quinones) is the final such transfer in the reaction center, and the one that is the most sensitive to perturbation, since Q_B is a readily exchangeable cofactor. The recovery of the ground state P absorption following laser flash excitation has characteristic lifetimes that depend upon the extent of completion of the photochemical sequence. Kinetics for laser flash-induced recovery of the 865 nm band measured both for RCs in the native, detergent-solubilized state and in the gel phase of the complex fluid are shown in Figure 3. Recovery of the 865 nm band in the native RCs was fit as a biexponential function, with 90% of the recovery having a lifetime of 0.9 s, corresponding to recombination from the final $P^+Q_B^-$ state, and the remainder having a lifetime of 60 ms, corresponding to recovery from the $P^+Q_A^-$. In the gel sample, 80% of the recovery was fit with a lifetime of 1.4 s, and the remaining 20% was fit with a 120 ms lifetime. The recovery kinetics indicate that extent of the final $Q_A^-Q_B \rightarrow Q_AQ_B^-$ electron transfer was diminished only by about 10% in the gel phase. The increase in the recovery times for the $P^+Q_B^-$ and $P^+Q_A^-$ in the gel phase is consistent with previous measurements that showed similar recovery times for RCs in high osmolarity media (7). These results indicate that the polymer-grafted, membrane-mimetic matrix has no adverse impact upon the electron and proton transfer activities of the RC.

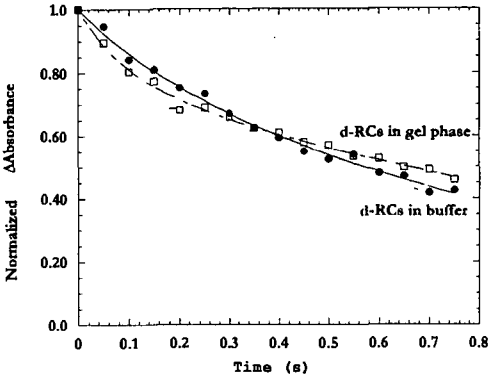

Figure 3. Kinetics for laser-flash induced recovery of the 865 nm band for RCs in 10mM Tris-100mM-NaCl-0.01%LDAO-0.01mM EDTA-pH7.8 buffer solution (solid circles) and in polymer-grafted membrane-mimetic gel (open squares).

To determine the effect of the introduction of RCs on the properties of the complex fluid, the response of the gel phase to addition of the RCs was examined by small angle X-ray diffraction. A typical SAXS pattern recorded for the complex fluid in the gel phase (at room temperature) is presented in Figure 4A. The pattern is dominated by four Bragg peaks of integral order (Q = 0.041, 0.083, 0.124, 0.164 $Å^{-1}$) and is indicative of a lamellar structure, that is, one consisting of alternating layers of water and organic components (Figure 1A). The first order Bragg peak corresponds to a periodicity of 153 Å. The effect of the incorporation of RCs (12 μm) into the gel phase is presented in Figure 4B. The SAXS profile shows the same periodic structure (*i.e.*, lamellar structure) as indicated by the integral order of the four observed Bragg peaks (Q = 0.035, 0.072, 0.108, 0.144 $Å^{-1}$). Some changes in the scattering pattern are apparent, however. First, the position of the first order Bragg peak indicates that the lattice spacing increases from 153 to 180 Å upon protein reconstitution. Second, introduction of RCs, which is believed to occur by insertion into the alkane region of the lipid bilayer, leads to both a reduction in the amplitude and an increase in the breadth of the diffraction peaks, suggesting a loss of spatial coherence and orientational disorder. This finding is consistent with prior work in which hydrophobic, dodecanethiol- derivatized gold nanoparticles, which selectively partition into the alkyl chains of the lipid/surfactant bilayer, were found to produce a similar effect on the observed SAXS profile (10).

Small angle neutron scattering (SANS) has also been used to assess the gels response to RC reconstitution and to obtain information regarding structural organization. Unlike X-ray scattering techniques, SANS permits determination of the structure of the fluid (cold) phase, by selective deuteration to highlight the aqueous channels (8). Previous, neutron scattering results yielded a low-resolution structure of the cold phase as normal hexagonal (5). Preliminary SANS investigations on complex fluid compositions incorporating reaction centers (data not shown) indicate that the cold phase structure changes to a cubic phase upon RC addition. Details of this analysis, along with results of studies employing deuterated reaction centers used to assess reaction center organization within these phases, will be presented in a future report (11).

CONCLUSIONS

The results presented here indicate that introduction of bacterial photosynthetic reaction centers into the polymer-grafted lipid-based complex fluid has no adverse impact on the structural or functional integrity of the protein. Preliminary investigations indicate that RC reconstitution does alter the structural organization of the complex fluid below the phase transition temperature (from a 2-D hexagonal array of prolate micelles to a 3-D cubic structure of micelles). Conversely, this introduction does not appreciably alter the structural properties of the gel phase of the complex fluid. Taken together, these results demonstrate that the complex fluid provides a medium of great potential utility in which to conduct fundamental investigations of protein structure and function.

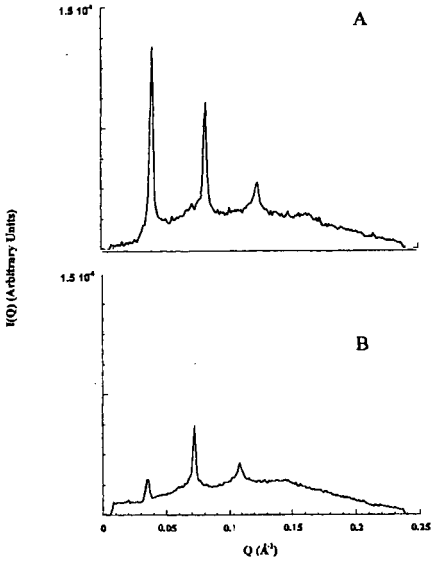

Figure 4. Small angle X-ray scattering profiles of (A) gel phase of the complex fluid, (B) gel phase incorporating 12 μm RCs.

ACKNOWLEGMENTS

The authors would like to thank Dr. Hiro Tsurata (SSRL) for his help in using the scattering instrument at beamline 4-2 (SSRL). This work was supported by the U. S. Department of Energy, Office of Basic Energy Sciences, Division of Chemical Sciences, under contract W-31-109-Eng-38.

REFERENCES

1. (a) Scaiano, J.C.; Garcia, H. *Acc. Chem. Res.* **1999**, *32*, 783. (b) Willner, I.; Willner, B. *Top. Curr. Chem.* 1991, 159. (c) Fox, M. A. *Top. Curr. Chem.* 1991, 67.

2. (a) Weidemaier, K.; Tavernier, H. L. Chu, K. T.; Fayer, M. D. *Chem. Phys. Lett.*, **1997**, *276*, 309. (b) Suguru, H.; Datsura, N.; Shin-ichi, S.; Yotaro, M.; Hiroshi, I.; Takahiro, K.; Yoshiteru, S. *Chem. Lett.* **1999**, *3*, 191. (C) Behera, G. B.; Mishra, B. K.; Behera, P. K.; Panda, M. *Adv. Colloid Interface Sci.* **1999**, *82*, 1.

3. Feher, G.; Allen, J. P.; Okamura, M. Y.; Rees, D. C. *Nature* , **1989**, *339*, 111.

4. Utschig, L. M.; Ohigashi, Y..; Tiede, D. M.; Thurnauer, M. C. *Biochemistry* **1998**, *37*, 8278.

5. Firestone, M. A.; Thiyagarajan, P.;. Tiede, D. M. *Langmuir*, **1998**, *14(17)*, 4688.

6. Marone, P. A.; Thiyagarajan, P.; Wagner, A. M.; Tiede, D. M. *J. Crystal. Growth*, **1998**, *191*, 811.

7. Tiede, D. M.; Vazquez, J.; Cordova, J.; Marone, P. A. *Biochemistry*, **1996**, *35*, 10763.

8. Firestone, M. A.; Tiede, D. M.; Thiyagarajan, P. in Materials Research Using Cold Neutrons at Pulsed Neutron Sources; Thiyagarajan, P.; Trouw, F.; Marzec, B.; Loon, C.-K., Eds.; World Scientific Publishing Co.: New Jersey, **1999**,160.

9. Thiyagarajan, P.; Epperson, J. E.; Crawford, R. K.; Kippert, T. E.; Wozniak, D. G. *J. Applied Cryst.* **1997**, *30*, 280.

10. Firestone, M. A.; Rajh, T.; Makarova, O. V.; Seifert, S.; Teide, D. M.; Nedelijkovic, J. M. submitted to *Polymer Preprints*.

APPLICATIONS OF X-RAY METHODS TO SPECIATE MANGANESE PARTICULATES FROM VEHICLES USING MMT FUEL

John G. Reynolds, and Art J. Nelson
Lawrence Livermore National Laboratory
Livermore, CA
J. Roos,
Ethyl Corporation, Richmond, VA

INTRODUCTION

Methylcyclopentadienyl manganese tricarbonyl (MMT) has been used as a fuel additive in both gasoline and diesel fuel [1]. Testing of fuels with this additive has been performed on a variety of makes and models of auto and diesel vehicles. These studies have been conducted with fuel containing MMT at a concentration of 0.03125 gram manganese per gallon. X-ray techniques (such as XAS and XPS) have been applied to samples of particulates collected from these test vehicles and engines to speciate the Mn and other metal compounds found in these exhaust particulates. Mn species such as phosphates, sulfates and oxides have been found in varying concentrations depending upon the make and model, the type of fuel, and the test conditions.

EXPERIMENTAL

Samples and techniques have been described in detail elsewhere [2]. The samples were collected using a Moudi Impactor on vehicles operated over the Urban Dynamometer Driving Schedule using a modification of the dilution tunnel technique described in 40 CFR Part 86. Seven samples were examined taken from five different vehicles: 92BR-TP (1992 Buick Regal Tailpipe), 93FE-TP (1993 Ford Escort tailpipe), 93FE-EO (1993 Ford Escort engine out), 93HC-TP (1993 Honda Civic tailpipe), 93HC-CO (1993 Honda Civic after catalytic converter), 93HC-TP (1993 Toyota Camry tailpipe), 93TCWOC-TP (1993 Toyota Camry without catalytic converter).

RESULTS

The approach for speciation of the Mn components employed the model compound technique. The selection of model compounds was based on knowledge of the behavior of Mn compounds in oxidative environments. The XPS and/or XAS spectra were taken on the samples and compared with spectra taken on the model compounds under the same conditions. Table 1 shows selected Mn, S, P, and O XPS parameters for the model compounds used in this study. Table 2 shows the XPS parameters for the particulate samples.

Table 1. Values of Binding Energies and Auger Parameter (in eV) for Manganese Model Compounds.

Sample	Mn $2p_{3/2}$	FWHM[a]	ΔMn 3s	Mn LMM[b]	α[c]	O 1s	S 2p	P 2p
Mn	639.0	1.40	3.4	586.5	-28.1	–	–	–
MnO	640.9	2.34	6.0	582.9	-29.8	529.8	–	–
Mn_3O_4	640.7	2.49	5.8	583.7	-29.2	529.5	–	–
Mn_2O_3	641.0	2.02	5.7	583.6	-29.0	529.5	–	–
MnO_2	641.7	2.50	4.8	583.8	-28.1	529.3	–	–
$MnSO_4$	641.8	2.39	6.3	581.2	-30.6	531.9	168.6	–
MnS	640.4	2.03	5.7	584.4	-28.8	–	160.9	–
$MnPO_4$	641.9	2.35	6.3	581.0	-30.7	531.8	–	133.9
Hureaulite[d]	641.5	2.11	6.3	581.3	-30.8	531.1 532.4	–	133.5
$Mn_2P_2O_7$	641.7	2.43	6.3	580.8	-31.1	531.5	–	133.9
$Mn_3(PO_4)_2$	641.7	2.04	6.3	581.2	-30.7	531.6	–	133.5

a) Full width half-maximum of Mn $2p_{3/2}$ peak in eV.
b) Kinetic energy of Mn $L_3M_{2,3}M_{4,5}$ Auger peak.
c) Auger parameter, $\alpha = BE + KE - 1253.6$ eV.
d) $Mn_5(PO_4)_2[PO_3(OH)]_2 \cdot 4H_2O$.

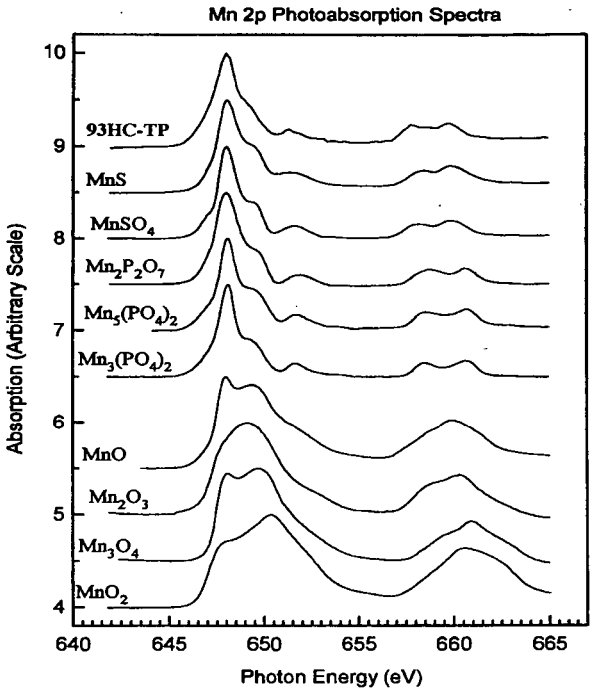

Figure 1. XAS spectra of selected Mn model compounds and the 1993 Honda Civic Tailpipe particulate sample.

Table 2. Binding Energies (in eV) of Major Elements Found in Particulate Emissions Collected on Cu and Au Foils.

Sample	Mn $2p_{3/2}$	α^a	C 1s	O 1s	S 2p	P 2p
93HC-TP	641.8		284.5	529.9 531.5 532.8	163.4, 167.9	133.5
93HC-CO	641.7	-31.6	284.3	530.1 531.4 532.2	161.7, 162.9	133.4
92BR-TP	642.0		284.6	530.2 532.2 534.0	163.0, 169.1	133.9
93FE-TP	642.3		284.8	530.9 532.6	161.6, 163.6 166.9, 169.6	133.7
93FE-EO	641.9		284.5	532.2	161.6, 163.1	130.8 133.6
93TC-TP	641.9	-29.9	284.7	532.3	163.2, 169.4	133.6
93TCWOC-TP	642.0	-30.5	284.8	530.6 532.1 533.6	163.2, 168.1	130.7 133.7

a) Auger parameter, α = BE + KE – 1253.6 eV.

Comparisons of the model compounds with the auto emission samples show that, in general, the particulates contain Mn phosphates, sulfates, and oxides.

Figure 1 show the XAS L-edge spectra of several Mn model compounds, one of the auto samples. Table 3 shows a summary of the XAS parameters for the model compounds, including energy shift, L_3 Linewidths and Branching ratios. Table 4 shows these parameters determined from the XAS L-edge spectra of the auto samples.

Table 3. Summary of the Mn L-edge Spectral Features for Selected Mn Compounds.

Compound	Mn Valency	$\Delta E(L_3 - L_2)$ (eV)	L_3 Linewidth FWHM (eV)	Branching Ratio $I(L_3)/I(L_3 + L_2)$
MnO_2	IV	10.1	5.5	0.65
Mn_3O_4	II, III	12.9, 11.5	4.1	0.68
Mn_2O_3	III	11.5	3.9	0.68
MnO	II	12.1	4.0	0.70
$Mn_3(PO_4)_2$	II	12.9	1.2	0.85
Hureaulite[a]	II	12.9	1.3	0.83
$Mn_2P_2O_7$	II	12.9	1.5	0.85
$MnSO_4$	II	11.9	1.3	0.85
MnS	II	11.9	1.6	0.84

a) $Mn_5(PO_4)_2[PO_3(OH)]_2 \cdot 4H_2O$.

Table 4. Summary of the Mn L-edge Spectral Features for Particulate Emissions Collected on Cu and Au Foils.

Sample	Estimated Average Mn Valency	$\Delta E(L_3 - L_2)$ (eV)	L_3 Linewidth FWHM (eV)	Branching Ratio $I(L_3)/I(L_3 + L_2)$
93HC-TP	II	11.9	1.7	0.85
92BR-TP	II	11.9	1.6	0.86
93FE-TP	II	11.9	1.8	0.84
93TCWOC-TP	II	11.9	1.5	0.85
93TC-TP	II	11.8	1.6	0.86

In agreement with the results from the XPS analyses, the predominant Mn species found in the particulate samples are Mn phosphates, sulfates, and oxides.

CONCLUSION

The XPS and XAS L-edge characterization of particulate emission samples taken from several automobiles operating with MMT in the fuels and in the UDDS mode show that the predominant Mn species are phosphates, sulfates, and oxides.

ACKNOWLEDGMENT

This work was performed under the auspices of the U.S. Department of Energy by the Lawrence Livermore National Laboratory under contract No. W-7405-ENG-48.

REFERENCES

[1]. J. E. Faggan, J. D. Bailie, E. A. Desmond, D. L. Lenane, SAE Paper 750925, Warrenville, PA, Society for Automobile Engeneering (1975). D. P. Hollrah, and A. M. Burns, *Oil and Gas J.* March 11, **1991**, pp 86–90.

[2] C. Colmenares, S. Deutsch, C. Evans, A. J. Nelson, L. J. Terminello, J. G. Reynolds, J. W. Roos, and I. L. Smith. *Applied Surface Sci.*, **1999**, 151, 189–202.

STRUCTURE OF ACTIVATED CARBONS PRODUCED FROM PAPER MILL SLUDGE USING SMALL ANGLE NEUTRON SCATTERING

[1]Giselle Sandí*, [2]Nasrin R. Khalili, [3]Kenneth C. Littrell, and [3]P. Thiyagarajan

[1]Chemistry and [3]Intense Pulsed Neutron Source Divisions, Argonne National Laboratory, 9700 South Cass Ave., Argonne, IL 60439; [2]Department of Chemical and Environmental Engineering, Illinois Institute of Technology, Chicago, Illinois 60616

ABSTRACT

A novel, cost-effective, and environmentally benign process was developed to produce highly efficient carbon-based adsorbents (CBAs) from paper mill sludge. The production process required chemical activation of sludge using zinc chloride and pyrolysis at 750°C in N_2 gas. The produced CBAs were characterized according to their surface area and pore size distribution using N_2-BET adsorption isotherm data. Further characterization of the surface and pore structure was conducted using small angle neutron scattering (SANS). The structural features analyzed by SANS revealed the dependence of porosity on zinc chloride concentration. The presence of inaccessible pores was also determined by solvent contrast-variation SANS experiments.

KEYWORDS: SANS, carbon-based adsorbents, paper mill sludge, porosity.

INTRODUCTION

A series of novel carbon-based adsorbents (CBAs) have been produced from paper mill sludge. The significant feature of the produced sludge-based activated carbon, that makes it a unique and particularly economical adsorbent/catalyst/catalyst support system, is that waste materials are used for its production. The produced CBAs can be extensively used as adsorbents, catalysts and catalyst supports in a variety of industrial and environmental applications (such as purification processes, recovery of chemical products, and removal of organic and metals). Their adsorption capability and catalytic activity are largely controlled by their surface characteristics [1,2]. For example, carbons used for the adsorption of gases and vapors should have pores with effective radii considerably smaller than 16-20 Å [2], while activated carbons with pore sizes in the range of 20-500 Å have been shown to be significant adsorbents for the removal of coloring impurities from liquid phase systems [3]. The relationship between the surface properties of activated carbon and its effectiveness as an adsorbent or catalyst, emphasizes the importance of developing methodologies by which activated carbon with specified surface properties can be produced.

Analysis of the surface physical properties of the produced carbons initially included determination of the total surface area, extent of microporosity, and characterization of the pore size distribution using nitrogen adsorption isotherms data [2, 3, 4]. While the results of the surface analysis have shown that activation methodology used to produce novel CBAs has a significant impact on the surface structure and performance of the carbons produced, these data alone were not sufficient to draw definite conclusions about the extent of correlation between the carbons' microporous structure and the activation methodologies employed in their production. Therefore, small angle neutron scattering (SANS) was used to supplement existing analysis and provide valuable information about the microscopic structures of the carbons produced. such as produced pore distribution, pore width, pore radii, characteristic lengths, and voids. The SANS data were used to study the surface properties of the carbons at mesoscopic length scales and to characterize their microstructure by determining the sizes and geometries of the component clusters and through solvent contrast variation, the accessibility of their micropores to solvent.

This information is fundamental for the characterization of these carbons and evaluation of the extent of availability of their pores to adsorbates in gas and/or liquid phase environments.

EXPERIMENTAL

The raw paper mill sludge was first dried in an oven at 110°C for 24 hours, then crushed mechanically using a paint-mixing machine. Crushing provided smaller particles with increased surface area and also enabled more efficient chemical activation of the raw material. Samples were sieved after mechanical crushing to obtain particle with sizes smaller than 600 μm. This particle size range was found to be the most suitable for the chemical activation process that was performed using five different $ZnCl_2$ to dried sludge mass ratios of 0.75, 1.0, 1.5, 2.0, and 2.5 [5]. To ensure a complete reaction between $ZnCl_2$ and sludge particles, sludge was mixed with zinc chloride at 85°C for 7 hours. After chemical activation, samples were dried in air at 110°C for 24-36 hours. The time required for drying varied depending on the amount of zinc chloride used for the activation process (i.e., higher impregnation ratios required longer drying time). After drying, the sludge was crushed again into a fine powder. Chemically activated samples were exposed to light and humidity (L&H) for about 22 hours to enhance the development of the pore structure during pyrolysis [5].

Pyrolysis of the chemically activated and L&H-treated sludge was carried out in an inert environment (70ml/min flow of nitrogen gas) at 800°C for two hours. Upon completion of the pyrolysis, the sample was removed from the reactor and crushed using a mortar and a pestle. The crushed samples were then cleansed using 500 ml of 1.2 M HCl followed by 500 mL of distilled water to remove excess zinc chloride and residual inorganic matter. After drying in air, the samples were transferred to 20-mL vials for storage prior to conducting the physical activation process. During the physical activation, samples were heated for two hours at 800 °C in a mixture of 75% CO and 25% CO_2. Upon completion of the physical activation, the produced carbons were characterized according to their surface properties by BET and related measurements.

For the SANS measurements, the carbons were ground into a powder. The SANS measurements at the SAND time-of-flight SANS instruments at the Intense Pulsed Neutron Source at Argonne National Laboratory [6] using cylindrical Suprasil sample containers with a neutron optical path length of 1 mm. SAND provides data in a Q range of 0.004 to 0.6 $Å^{-1}$ in a single measurement. All samples were studied as dry powders. Additionally, a contrast-variation SANS study was performed on the sample treated with the highest zinc chloride ratio by preparing the powdered sample as slurries in mixtures of normal and deuterated toluene with deuterated toluene proportions of 0, 25, 50, 75 and 100 %. In preparing the slurries, the powder was slowly evacuated to avoid air bubble formation prior to adding the solvent. The scattering from an empty cell was used for background correction in these measurements.

RESULTS AND DISCUSSION

The SANS data for the dry powder samples was initially analyzed by using a modified version of the unified Guinier analysis and power law model proposed by Beaucage et al. [7, 8] to fit the full range of the data. As shown in Table 1, the results of this unified fit indicate that at the lowest Q scale, the behavior all of the dry powder carbon samples except the one prepare with a 0.75/1 $ZnCl_2$ ratio is that of surface-fractal interfaces of large objects. However, the low Q fractal dimension of ~4 obtained for the 0.75/1 $ZnCl_2$ ratio sample is characteristic of a smooth interface. At higher Q and thus shorter length scales, the power law exponents obtained were consistent with those from mass fractal aggregates.

In order to gain a better understanding of the microstructure of these systems, we subtracted the low-Q power law behavior from the measured scattering curves, enhancing the visibility of features at higher Q, and fit the difference data using the model developed by Teixiera [9]. In this model, which describes the scattering from mass fractal aggregates of small, uniform spheres of radius R, the scattered intensity is given by:

$$I(Q;\xi,D_F,R) = I_{0S}\left(1+\frac{\sin[(D_F-1)\arctan(Q\xi)]}{(QR)^{D_F}\left(\frac{1}{Q^2\xi^2}+1\right)^{\frac{D_F-1}{2}}}\right)P_{Sphere}(Q;R)+I_{Background}$$

where D_F is the mass-fractal dimension, ξ is the exponential cutoff length for the aggregate, $I_{Background}$ is the background intensity, and I_{0S} is the intensity scattered by the fundamental sphere extrapolated to $Q=0$. Here,

$$P_{Sphere}(Q;R)=\left[\frac{3(\sin(QR)-QR\cos(QR))}{(QR)^3}\right]^2$$

is the scattering form factor for the fundamental sphere [10].

The data with the low Q power law scattering subtracted is compared with the fit functions in figure 1 and the corresponding fit parameters are given in Table1. The results of the Teixeira model fits to the data for the samples prepared with the three highest ratios of $ZnCl_2$ indicates that these samples are similar in their microstructure. For these samples, both the fractal dimension and the size of the aggregates as indicated by the exponential cutoff size parameter ξ increase as the $ZnCl_2$ ratio increases. However, the other two samples are significantly different in their microstructure. The sample prepared with a $ZnCl_2$ ratio of 0.75 has a much lower mass fractal dimension and a much larger extent. The sample prepared with a $ZnCl_2$ ratio of 1.0 has a mass fractal dimension close to 1 and is better fit by the form factor for a cylinder [10]. Similar behavior has also been observed in silica systems [11]. The size of the fundamental particle of which these aggregates are composed is found from the fits to be approximately 2 Å and is thus of nearly atomic size.

The same approach was used to analyze the data from the solvent contrast variation study performed using slurries of the sample with a $ZnCl_2$ ratio of 2.5 immersed in different mixtures of toluene and deuterated toluene. The results of the fits are presented in Table 2. The quality of the fits to the data with the low Q power law behavior subtracted is shown in figure 2. The low-Q power law of this sample in 100% D-toluene was that of a mass fractal while all of the other samples had surface-fractal power-laws. Similarly, while the other four samples were well described by the Teixeira mass fractal model at high Q, the data for the sample in 100% deuterated toluene is inconsistent with this model but well described as a polydisperse, nearly hollow shell. The change in the shapes of the scattering curves without loss of intensity at low Q seen in figure 2 for the three samples with the highest concentration of deuterated toluene indicates that the toluene solvent is unable to completely contrast-match the scattering length density of the aggregates. This suggests that the toulene is not able to completely penetrate the micropores in these samples.

CONCLUSIONS

This SANS study has shown that the microscopic structure of these activated carbons prepared from paper-mill sludge is sensitively dependent on the ratio of $ZnCl_2$ used in their preparation. The mass fractal dimensions observed for the samples prepared with higher ratios of $ZnCl_2$ are similar to each other and to the fractal dimension of 2.5 associated with growth by percolation and/or diffusion-limited aggregation. The parallel trends observed in BET analysis and the structural determination by small angle scattering for these samples shows that modifications of the production procedure can significantly and systematically alter the quality and characteristics of the final products. The lower fractal dimensions of the other two samples show that they are lower dimensional structures. The fitted fractal dimension was consistent with the rod-like structure observed for the sample prepared with $ZnCl_2$/sludge ratio of 1.

The small pore structure of these carbons suggests that they can be used in a variety of gas-phase cleaning applications. Further studies of the catalytic and adsorbate properties of these activated carbons and others similar to them correlated with these studies of their microstructure and mesoscopic surface structure will allow for the production procedure to be systematically tailored to produce activated carbons that are optimized for performance in a variety of applications.

ACKNOWLEDGMENTS

This work has benefitted from the use of the Intense Pulse Neutron Source at Argonne National Laboratory, and was performed under the auspices of the U.S. Department of Energy, Office of Basic Energy Sciences, Division of Chemical Sciences, under contract number W-31-109-ENG-38.

REFERENCES

[1] Bansal, R. C.; Donnet, J.; Stoeckli, F. *Active Carbon,* NY:New York City, **1988**.
[2] Boppart, S.; Ingle, L.; Potwora, R. J.; Rester, D. O. *Chemical Processing* **1996**, 79.
[3] Walker, P. L. *Chemistry and Physics of Carbon*, NY:New York City, **1996**.
[4] Campbell, M. MS thesis, Illinois Institute of Technology, **1998**.
[5] Khalili, N. R. IIT Patent #147, **1999**.
[6] Thiyagarajan, P.; Epperson, J. E.; Crawford, R. K.; Carpenter, J. M.; Klippert, T. E; Wozniak.; D. G. *J. Appl. Cryst.* **1997**, *30*, 280.
[7] Beaucage, G. *J. Appl. Cryst.* **1996**, *29*, 134.
[8] Beaucage, G. *J. Appl. Cryst.***1995**, *26*, 717.
[9] Teixeira, J. J. Appl. Cryst. **1988**, *21*, 781.
[10] Pedersen, J. S. *Adv. Colloid Interface Sci.*, **1997**, *70*, 171.
[11] Hyeon-Lee, J.; Beaucage, G.; Pratsinis, S. E. *Chem. Mater.* **1997**, *9*, 2400.

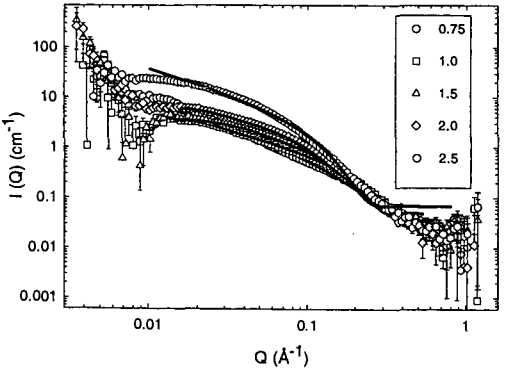

Figure 1: Resulting SANS plots after subtraction of the low Q power law. The solid lines indicate the fit to the Teixeira model.

Table I: Results of the Teixeira sphere mass fractal fit to the samples shown in figure 1.

$ZnCl_2$/sludge ratio	BET surface area (m^2/g)	Low Q Power Law Exponent	High Q Fractal dimension	Cutoff Length ξ (Å)
0.75	895	-4.02 ± 0.04	1.37 ± 0.01	NA (too large)
1.0*	1015	-3.46 ± 0.02	1.19 ± 0.02	67 ± 4
1.5	1067	-3.59 ± 0.01	2.18 ± 0.02	15.6 ± 0.3
2.0	1095	-3.70 ± 0.01	2.36 ± 0.02	17.2 ± 0.2
2.5	1249	-3.52 ± 0.02	2.50 ± 0.01	23.4 ± 0.2

* This data set was better fit by the form factor for a cylinder of radius 7.84 ± 0.09 Å and length 179.6 ± 4.8 Å.

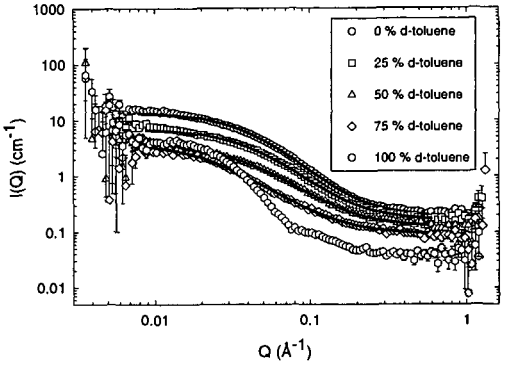

Figure 2: SANS plots of $ZnCl_2$/sludge ratio of 2.5, immersed in different toluene/d-toluene mixtures.

Table II: Results of the Teixeira sphere mass fractal fit to the samples shown in figure 2.

2.5 $ZnCl_2$/sludge ratio Sample in	Low Q Power Law Exponent	High Q Fractal dimension	Cutoff Length ξ (Å)
0 % d-toluene	-3.64 ± 0.03	2.42 ± 0.01	23.6 ± 0.2
25 % d-toluene	-3.70 ± 0.06	2.35 ± 0.02	22.6 ± 0.4
50 % d-toluene	-3.67 ± 0.11	2.26 ± 0.03	23.1 ± 0.7
75 % d-toluene	-3.29 ± 0.11	2.03 ± 0.04	46.5 ± 2.1
100 % d-toluene	-2.82 ± 0.04	NA	NA

SPECIATION OF NICKEL IN RESIDUAL OIL FLY-ASH BY XAFS SPECTROSCOPY

Frank E. Huggins[1], Gerald P. Huffman[1], Kevin C. Galbreath[2], Donald L. Toman[2], and John L. Wong[3]

[1]Chemical and Materials Engineering/CFFLS, University of Kentucky, 533 South Limestone Street, Suite 111, Lexington, KY 40506-0043, fhuggins@engr.uky.edu

[2]Energy & Environmental Research Center, University of North Dakota, P.O. Box 9018, 15 North 23rd Street, Grand Forks, ND 58202-9018

[3]Department of Chemistry, University of Louisville, 2320 South Brook Street, Louisville, KY 40292

KEYWORDS: Residual oil, nickel speciation, XAFS spectroscopy

ABSTRACT

The US EPA has recently expressed concern about the possible presence of carcinogenic nickel subsulfides (*e.g.* Ni_3S_2, *etc.*) in fly-ash generated and released during combustion of residual oil for power generation. To examine the forms of nickel in residual oil fly-ash samples, we have used a combination of X-ray absorption fine structure (XAFS) spectroscopy, X-ray diffraction, and a sequential extraction-anodic stripping voltammetry (ASV) technique. Differences were found in the nickel speciation between experimental (7 kW) and commercial (400 MW) combustion systems burning similar 0.85 wt% sulfur residual oils. Whereas almost all of the nickel was found to occur as nickel sulfate in the fly-ash from the experimental system, the fly-ash from the commercial system contained significant nickel in the form of a spinel phase, possibly $NiFe_2O_4$. No significant evidence was found for the occurrence of any nickel sulfides in any sample, suggesting the cancer risk from Ni in residual oil fly ash is greatly exaggerated.

INTRODUCTION

The combustion of residual (No. 6) fuel oil for steam generation has the potential to release significant quantities of various metals, specifically vanadium, nickel, and chromium, and the semi-metal, arsenic, into the atmosphere [1]. Further, unlike fly-ash products from coal combustion, which contain abundant aluminosilicates that can react with and sequester trace metals in relatively unreactive glassy forms, fly-ash products from residual oil combustion usually do not contain significant quantities of aluminosilicates and the occurrence of these metals in residual-oil fly-ash is principally as oxides or sulfur compounds, either sulfates or sulfides. In particular, there is much concern about the inhalation risk associated with nickel because of the potential for formation of highly carcinogenic nickel subsulfides (Ni_3S_2, *etc.*) in the fly-ash or fine particulate matter released during residual oil combustion [1]. Some limited nickel speciation analyses from power plants burning residual oil have reported as much as 26% of the Ni present as nickel subsulfides. However, it is possible that such values arise because of limitations in the indirect method used for speciating the nickel, *viz.*, sequential extraction-anodic stripping voltammetry (ASV).

In this investigation, we have used three complementary methods to examine the nickel speciation in residual oil fly-ash samples produced in laboratory- and commercial utility-scale combustion. These methods are nickel X-ray absorption fine structure (XAFS) spectroscopy, X-ray diffraction (XRD) and the sequential extraction-ASV technique. In addition, samples were measured by XAFS spectroscopy before and after the first step in the sequential-extraction procedure for a more direct comparison with the ASV method.

EXPERIMENTAL

(i) Sample collection

Laboratory fly-ash samples were generated by combustion of a 0.86 wt% sulfur residual oil in a bench-scale down-fired 7 kW combustion unit [2] at an excess O_2 concentration of about 3 mol%. In this unit, a peak temperature of about 1500°C was achieved for about 0.5 s after which the gas-stream was cooled at a rate of 600°C/s before being sampled at a temperature of 300°C. Commercial fly-ash samples were obtained by isokinetic sampling from the stack of a 400 MW boiler using a modified EPA method 17 sampling-train assembly [3]. Samples were collected on two consecutive days: on the first day, a 0.80 wt% sulfur residual oil was burnt; on the second day, a 0.88 wt% S residual oil was burnt. The temperature of sampling was approximately 290°C. Further details of the sampling are given in more detail elsewhere [4].

(ii) Sample analysis methods

Ni K-edge XAFS spectroscopy was carried out at either beam-line IV-3 at the Stanford Synchrotron Radiation Laboratory (SSRL), Stanford University, CA, or at beam-line X-18B at the National Synchrotron Light Source (NSLS), Brookhaven National Laboratory, NY. Similar experimental practice was carried out at both synchrotron sources. Ash samples were suspended in the monochromatic X-ray beam using ultra-thin polypropylene bags. Nickel XAFS spectra were collected from the ash samples in fluorescent mode using either a 13-germanium array detector [5] or a Lytle fluorescence detector [6], depending on the concentration of the nickel. XAFS spectra were typically collected at X-ray energies ranging from about 100 eV below to at least 600 eV above the nickel K absorption edge. A thin nickel metal foil was used as the primary calibration standard; where possible, the foil was run in an absorption experiment after the fluorescence experiment so that it provided a simultaneous calibration. The first major peak in the derivative of the absorption spectrum of the foil was assumed to define the position of the nickel absorption edge at 8,333 eV. In addition, XAFS spectra of a number of standard compounds of nickel were obtained in connection with this work. These spectra were obtained in absorption geometry from thin pellets using ionization detectors.

The XAFS data collected at the synchrotron were returned to the University of Kentucky for analysis. The data were analyzed in the usual fashion [7,8]: after calibration of the energy scale, the spectra were split into separate X-ray absorption near-edge structure (XANES) and extended X-ray absorption fine structure (EXAFS) regions and each region was analyzed separately. The XANES region was used as a fingerprint for identification of the forms of occurrence of nickel in the fly-ash samples. The EXAFS region was mathematically manipulated in the usual manner [7,8] to yield the radial structure function (RSF), which is basically a one-dimensional representation of the local structure around the nickel in the material under investigation.

X-ray diffraction (XRD) was carried out on a Phillips XPert diffractometer system at the University of North Dakota using Cu K_α radiation, a step-size of 0.02° 2θ, and a time of 1 s/step. Diffraction patterns were collected over a range of 2θ from 5 to 70°. Samples were ground in an agate mortar and pestle and mounted on quartz plate for the XRD analysis.

Sequential extraction-ASV analysis was performed at the University of Louisville. Although a five-step extraction sequence has been developed for determining nickel speciation in oil fly-ash [9], only the first step, designed to separate soluble nickel compounds from the residual oil fly-ash, was performed in this work. This step involved extracting the ash samples in a 1.0 M sodium acetate – 0.5 M acetic acid solution buffered at pH 5 in an 8 mL centrifuge tube and bubbled with nitrogen for 10 minutes. The capped tube was then sonicated in a water bath for 2 hours at 25°C and centrifuged at 10,000 rpm for 20 minutes. Nickel in the supernatant was quantified by ASV of nickel dimethylglyoxime collected on a hanging Hg drop electrode with a CH-620 electroanalytical system in square-wave voltammetry mode. Nickel concentrations were obtained by the standard additions method. The residue remaining in the centrifuge tube was repeatedly extracted until Ni was not detected in the supernatant. At this point it was assumed that all soluble nickel compounds had been removed from the fly-ash.

RESULTS AND DISCUSSION

(i) XRD Analysis

X-ray diffraction analysis detected abundant amorphous components (glass, unburnt carbon) and anhydrite ($CaSO_4$) in all three fly-ash samples. In addition, the laboratory fly-ash sample contained gypsum ($CaSO_4.2H_2O$) and glauberite, ($Na_2Ca(SO_4)_2$), whereas the commercial fly ash sample collected on the first day of sampling contained hexahydrite ($MgSO_4.6H_2O$), periclase (MgO) and tentatively spinel, and that collected on the second day contained sodalite, ($(Na,Ca)_{4-8}Al_6Si_6O_{24}(SO_4,Cl)_{1-2}$), and maghemite, ($\gamma$-$Fe_2O_3$). The magnesium phases are likely to have arisen from reaction and decomposition of brucite ($Mg(OH)_2$) that was added to the oil to mitigate formation of free H_2SO_4 in the boiler. No nickel phases were specifically identified.

(ii) Acetate Extraction-ASV Analysis

The acetate extraction-ASV analysis divided the nickel into two fractions in each of the fly-ash samples: soluble nickel and insoluble nickel. For the laboratory fly-ash sample, 80% of the nickel was found to be present in soluble forms and the remainder in insoluble forms. For the two commercial fly-ash samples, significantly smaller fractions of the nickel were found to be present in soluble forms: for the Day 1 sample, 51%, and for Day 2 sample, 28%. In addition,

the total nickel concentration was found to be quite different between the laboratory and commercial fly-ash samples, *viz.*, about 0.4 wt % and about 2.0 wt%, respectively.

(iii) XAFS Spectroscopy

The nickel XANES and RSF spectra of the laboratory fly-ash are shown in Figure 1. The RSF exhibits one major peak at a phase-shift uncorrected distance, 1.61 Å, consistent with Ni-O distances, and the overall shape of the XANES spectrum is also consistent with bonding of the nickel to oxygen anions [10]. Based on comparison of the fly-ash XANES and RSF spectra with those of various nickel standard compounds [10], the best match was found to be a hydrated nickel sulfate ($NiSO_4.xH_2O$). The nickel XAFS data did not change significantly after the acetate extraction process, even though about 80% of the nickel was extracted. This indicates that the nickel is almost entirely present as nickel sulfate. Additionally and most significantly, there is no enhancement of any spectral features that can be attributed to nickel subsulfides, which, if they had been present to any significant extent in the fly-ash, should have been five times more prominent in the spectra of the extracted sample.

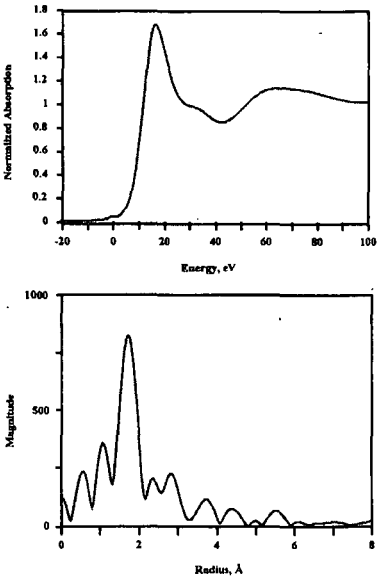

Figure 1: Ni XANES (top) and RSF spectra (bottom) for fly-ash generated in the laboratory from combustion of residual (No. 6) oil. The spectra did not change significantly after the acetate extraction.

The corresponding spectra for the commercial fly-ash sample collected on the first day are shown in Figure 2, both before and after the acetate extraction. Quite similar spectra were

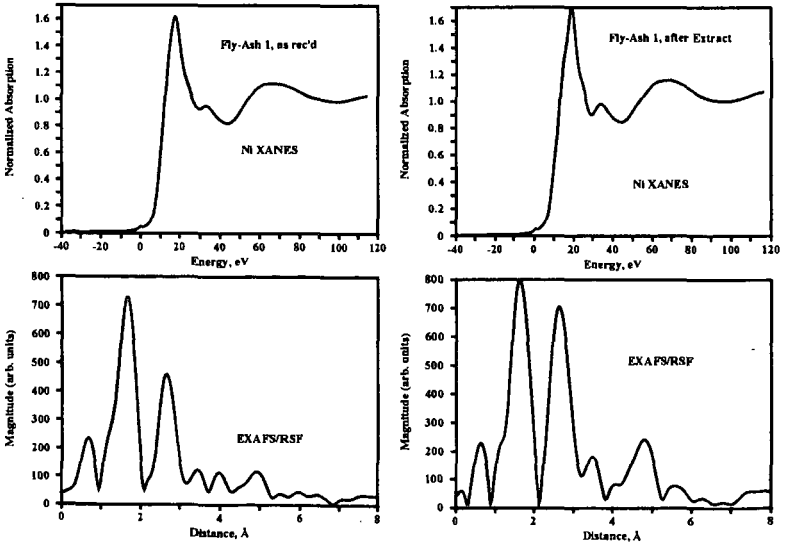

Figure 2: Ni XANES and RSF spectra for the residual oil fly-ash sample collected on day 1 at a commercial power plant, before (left) and after (right) extraction in a sodium acetate/acetic acid solution.

obtained from the fly-ash sample collected on the second day. As can be seen, there are significant differences in comparison with the spectra for the laboratory fly-ash sample and also between the spectra before and after the acetate extraction. In particular, the broad peak in the XANES spectrum at about 30-40 eV is more prominent and there is a second major peak in the

RSF spectrum at about 2.7 Å in the fly-ash samples from the commercial power plant. Both features become even more prominent after the acetate extraction.

Our first attempt at interpretation of the nickel XAFS data for the commercial fly-ash samples was in terms of a mixture of nickel sulfate ($NiSO_4$) and nickel oxide (NiO). Of the measured standard spectra that we had examined up to that point [10], only NiO had features in its XANES and RSF spectra that were consistent with the enhanced features shown in the corresponding spectra of the commercial fly-ash samples. However, the height ratio of the peaks at 1.6 and 2.7 Å, $A_{1.6}/A_{2.7}$, in the NiO RSF (Figure 3) is much different from that exhibited by the fly-ash and to explain the spectral data on the basis of a mixture of nickel sulfate and nickel oxide we would have to conclude that either (i) the acetate extraction removed only a very small fraction of the nickel as nickel sulfate, contrary to the results from the acetate extraction-ASV data, or (ii) that the reduction in the peak height ratio in the RSF was due to NiO of very small size. Neither of these explanations appeared very satisfactory.

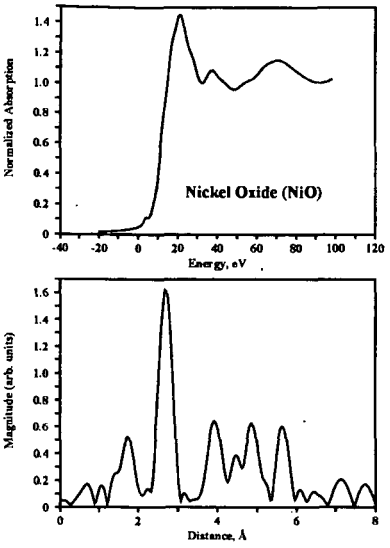

Figure 3: Nickel XANES (top) and RSF (bottom) for nickel oxide (NiO).

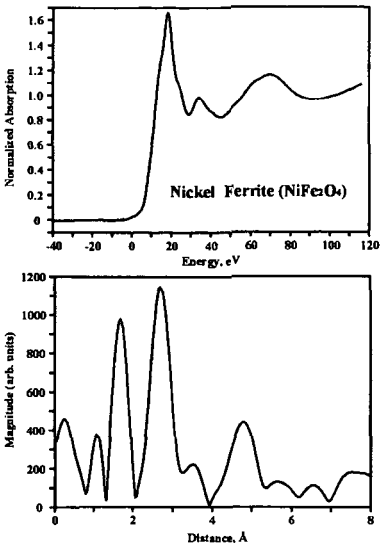

Figure 4: Nickel XANES (top) and RSF (bottom) for synthetic nickel ferrite ($NiFe_2O_4$).

The XRD patterns for the fly-ash, however, had suggested the possible presence of a spinel phase and nickel is known to enter spinel compounds readily. Hence, the possibility was explored that nickel might be present as a spinel oxide in the fly-ash samples. A sample of the nickel spinel, nickel ferrite ($NiFe_2O_4$), was synthesized at high temperature at the University of North Dakota by reacting stoichiometric amounts of NiO and α-Fe_2O_3 at 1600°C and 1400°C for 2 hours and 3 hours, respectively, in air. The purity of the spinel was confirmed using XRD; the measured cell parameter for this cubic material was 8.331 ± 0.006 Å in agreement with the value of 8.339 Å reported in the Powder Diffraction file No. 10-325 for $NiFe_2O_4$. The XAFS spectrum was then acquired in absorption geometry from a pressed pellet of the synthesized $NiFe_2O_4$ diluted in SOMAR mix. The Ni XANES and RSF spectra for the spinel are shown in Figure 4.

Comparison of the spectral data for $NiFe_2O_4$ with the data for the fly-ash samples provides a much better explanation than that for NiO. Not only is the ratio of the major peaks in the RSF of nickel ferrite much closer to that observed in the spectra of the extracted fly-ash samples, but the presence of a broad peak at about 4.8 Å in the RSF of nickel is also duplicated in the fly-ash spectra, especially those of the extracted samples. It is conceivable that the small differences in the height ratios of the major RSF peaks for the nickel ferrite standard and the extracted samples can be explained by the presence of aluminum or other light element substituting for the ferric iron in the spinel found in the commercial fly-ash. Hence, we do not now have to postulate that the acetate extraction incompletely removed the nickel sulfate, although that certainly remains a possibility, in light of the result obtained for the laboratory fly-ash. Regardless, the XAFS spectra of the extracted residues can be interpreted as arising from a substituted nickel-iron spinel as the predominant nickel-bearing phase.

Although less certain than for the laboratory fly-ash sample, there is no evidence from the XAFS data that there is any significant nickel sulfide species present in either of the commercial fly-ash

samples or their acetate extracts. Simulation of XANES spectra of hypothetical mixtures of the laboratory fly-ash and nickel sulfide (NiS) indicates that it should be possible to recognize a 5-10% occurrence of a nickel sulfide species in a fly-ash sample containing predominantly nickel sulfate species. The fact that spectral features attributable to nickel sulfides are not observed either for the fly-ash samples or their extraction residues indicates that such species are not significant and certainly less than 5% of the total nickel in the fly-ash.

CONCLUSIONS

XAFS spectroscopy, supplemented by results from XRD and acetate extraction-ASV techniques, indicates that hydrated nickel sulfate is the major nickel compound present in laboratory-generated residual oil fly-ash samples, whereas nickel-containing spinel is a significant second component in commercial fly-ash samples obtained from combustion of residual oils of similar sulfur contents. As discussed elsewhere [4], it would appear that the magnesium hydroxide added to the commercial residual oil to prevent formation of free sulfuric acid in the boiler promotes the formation of nickel spinel by providing additional cation species that compete in reacting with the acidic sulfur species. In none of the fly-ash samples was there any evidence for the presence of nickel sulfides. This result suggests that the EPA's estimate of the nickel inhalation cancer risk from residual oil-fired utilities, which is based on the assumption that the nickel species emitted by such utilities have 50% of the cancer potency of nickel subsulfide [1], could be overestimated by as much as a factor of 10.

ACKNOWLEDGEMENTS

This work was jointly sponsored by a consortium consisting of the American Petroleum Institute, Amerada Hess Corporation, Electric Power Research Institute, Florida Power & Light Company, Hawaiian Electric Corporation, and Public Service Electric and Gas Company, and the Center for Air Toxic Metals at the University of North Dakota Energy & Environmental Research Center. The Center for Air Toxic Metals is supported by the U.S. Environmental Protection Agency. Dr. E. Zillioux and co-workers from Florida Power & Light Company are acknowledged for expediting the fly-ash sampling at the 400-MW power plant. The U.S. Department of Energy is acknowledged for its support of the synchrotron facilities at Stanford University, CA, and Brookhaven National Laboratory, NY.

REFERENCES

[1] Environmental Protection Agency, *Study of Hazardous Air Pollutant Emissions from Electric Utility Steam Generating Units—Final Report to Congress, Volume 1.* EPA Report EPA-453/R-98-004a, February 1998.

[2] S. Benson, J. Pavlish, C. Zygarlicke, T. Erickson, K. Galbreath, G. Schelkoph, E. O'Leary, R. Timpe, C. Anderson, *Center for Air Toxic Metals Year 2 and 3 Final Technical Report—Section 3.0 Process Impacts on Trace Element Speciation.* Energy & Environmental Research Center Publication 98-EERC-03-03, April 1998, pp. 13-66.

[3] Environmental Protection Agency, Emission Measurement Technical Information Center, Method 17, *Determination of Particulate Emissions from Stationary Sources (In-Stack Filtration Method).* http://www.epa.gov/ttnemc01/promgate/m-17.pdf, September 1998.

[4] K. C. Galbreath, D. L. Toman, C. J. Zygarlicke, F. E. Huggins, G. P. Huffman, J. L. Wong, *JAWMA*, submitted October 1999.

[5] S. P. Cramer, O. Tench, N. Yocum, G. N. George, *Nucl. Instrum. Meth.*, **A266**, 586-591, (1988).

[6] F. W. Lytle, R. B. Greegor, D. R. Sandstrom, E. C. Marques, J. Wong, C. L. Spiro, G. P. Huffman, F. E. Huggins, *Nucl. Instrum. Meth.*, **226**, 542-548, (1984).

[7] P. A. Lee, P. H. Citrin, P. Eisenberger, B. M. Kincaid, *Rev. Mod. Phys.*, **53**, 769-808, (1981).

[8] D. C. Koningsberger, R. Prins, *X-ray Absorption.* J. Wiley & Sons, New York, (1988).

[9] J. L. Wong, J. Qian, C. H. Chen, *Anal. Chim. Acta*, **349**, 121-129, (1997).

[10] K. C. Galbreath, D. L. Toman, C. J. Zygarlicke, F. E. Huggins, G. P. Huffman, J. L. Wong, *Energy & Fuels*, **12**, 818-822, (1998).

USING WAVELENGTH DISPERSIVE X-RAY FLUORESCENCE SPECTROMETRY TO MEASURE CATION SEQUESTRATION BY WOMBAT TIRE-DERIVED PARTICLES

David L. Wertz, E. Ryan Smith and Ashley D. Trahan

Department of Chemistry and Biochemistry
The University of Southern Mississippi
Hattiesburg, MS 39406-5043, USA

KEYWORDS: Cation sequestration, tire-derived particles

INTRODUCTION: Because wavelength-dispersive x-ray fluorescence (WDXRF) spectrometry may be utilized to examine a variety of condensed phase samples, it has been helpful to this group in our development of a tire processing technique called the WOMBAT -- for analysis of the black graining powder which is one product of the WOMBAT process. This powder, formed by degradation of the styrene-butadiene rubber in the tire, is dispersed in the mixed solvent prior to removal from the WOMBAT reactor and is separated from the mixed solvent by filtration and drying. This tire-derived powder is an important process component.

To a first approximation, the intensity of an analyte peak in the WDXRF spectrum of a multi-component sample is approximately proportional to the abundance of that analyte. This group has used a series of mixtures of solid state materials to approximate the abundances of key analytes (zinc, sulfur, and iron) in tires and in the tir-derived powders that have been produced from chemical degradation of the tires. The WDXRF spectrum of the WOMBAT solid tire-derived solid (TDP) contains a sulfur K_α peak which is smaller than the sulfur K_α peak (at 5.37 Å) in the untreated tire. The WDXRF spectrum of the black TDP powder is presented in Figure 1. The small zinc K_α peak (at 1.44 Å) in the WDXRF spectra of the tire-derived powder, when compared to the corresponding peak in the WDXRF spectrum of the untreated tire, indicates to ca. 95% of the zinc has been removed from the tire during our chemical processing. Using the same analysis procedure, the sulfur abundance is reduced by ca. 35% in the transition from the untreated tire to the TDP. The sulfur reduction produces a material, i.e., the TDP, which is a low polluting solid state fuel. However, the WDXRF spectrum of the TDP contains large iron peaks (K_β and K_α at 1.77 Å and at 1.94 Å, respectively) that are not present at such intensities in the WDXRF of the untreated SBR from the tire. The intensity of the Fe peaks in the WDXRF spectra of TDP is related to the length of time the TDP is allowed to remain in the reactor. The presence of the large iron peaks is consistent with the following reaction sequences:

- dissolution of iron from the steel belts into the reactor solution, and
- *in vivo* sequestration of the iron from the reaction solution by the TDP.

In order to determine if the TDP produced by the WOMBAT process is effective in sequestering other metal ions from solutions, small aliquots of the TDP have been introduced into aqueous solutions containing selected dissolved metal salts. Our results are presented below.

EXPERIMENTAL PROCEDURE: Five grams of TDP were dispersed into 100 ml of 0.1 molar aqueous solutions containing several reagent metal salts. After allowing the TDP to equilibrate, the TDP was separated from the aqueous solution by filtration, and then dried in a convective oven.

Each dried sample of treated TDP was then split into two parts. Part one was mounted onto a sample holder, and a WDXRF spectrum was obtained. Part two of each treated TDP sample was thoroughly washed with water and then recovered by filtration, dried, and mounted onto a sample holder. A schematic of the process is presented in Figure 2.

A wavelength dispersive x-ray fluorescence (WDXRF) spectrum of each sample was obtained using a Rigaku S-Max spectrometer equipped with an end-centered rhodium x-ray tube to cause elemental excitations and a graphite monochromator to disperse the secondary Xrays emitted by each sample during de-excitation. Each spectrum was obtained by collecting intensities for 4 second intervals between the angles of $2\theta = 8.00°$ and $2\theta = 140.00°$ at increments of $\Delta 2\theta = 0.05°$.

RESULTS: Shown in Figures 3-6 are the WDXRF spectra of the TDP recovered from the

aqueous solution containing Cu^{+2} [Cu-TDP], from the aqueous solution containing Cr^{+3} [Cr-TDP], from the aqueous solution containing Hg^{+2} [Hg-TDP], and from the aqueous solution containing Pb^{+2} [Pb-TDP], respectively. In all of these WDXRF spectra, the zinc peak characteristic of the TDP has become too low to be detected, but the iron peaks are clearly discernible and only slightly less intense than in the WDXRF spectrum of the untreated TDP. The peak(s) due to the metal ions sequestered onto the TDP are labeled in each figure.

Thus, the spectra obtained may be explained in the following manner:

- Large copper peaks, K_β at 1.39 Å and K_α at 1.54 Å, appear in this WDXRF spectrum.
- The L_β and L_α peaks due to mercury, at 1.05 Å and at 1.24 Å are quite large in the WDXRF spectrum of this sample.
- The L_β and L_α peaks for lead, at 0.98 Å and at 1.18 Å, are small but clearly discernible in that WDXRF spectrum.
- The K_α peak for chromium, at 2.25 Å, is small but discernible.

Based of qualitative evaluation of the metal ion peaks in these spectra, the spectra was be divided into two groups. In the spectrum of the copper-containing TDP and in the spectrum of the mercury-containing TDP, the analyte peaks are quite large. However, for the spectra of the lead-containing TDP and of the chromium-containing TDP, the analyte peaks are quite small.

In a sample containing several types of atoms, the K_α peak intensity for analyte A (at λ_A) is given by:

$$I_A(\lambda_A) = M(\lambda_A) \bullet \eta_A \bullet I_A(\lambda_A) \bullet \exp[-\{\mu_s(\lambda_{Rh}) + \mu_S(\lambda_A)\} \bullet t_s \bullet \rho_S]; \qquad (1)$$

where $\mu_s(\lambda_{Rh})$ is the mass absorption coefficient of the sample for the rhodium Xrays, $\mu_S(\lambda_A)$ is the mass absorption of the sample for the secondary Xrays emitted by analyte A contained in the sample of average thickness is t_s and density ρ_S. The abundance of analyte A is given by η_A, and $I_A^*(\lambda_A)$ is the absorption-free intensity for a pure sample of analyte A. $M(\lambda_A)$ described the efficiency of the spectrometer in measuring intensity at wavelength λ_A. For similar samples (P and Q) containing analyte A, a ratio of intensities measured from the WDXRF spectra of sample P and of sample Q may be used to estimate differences in the abundance of analyte A; i.e.,

$$I_{A\text{-}P}(\lambda_A) / I_{A\text{-}Q}(\lambda_A) \approx \eta_{A\text{-}P}/\eta_{A\text{-}Q} \qquad (2)$$

Shown in Figure 7 are the WDXRF spectra of the Cu-containing TDP before and after the thorough washing with distilled water. The intensity of the copper peaks is decreased by 75-80%. A smaller reduction in peak intensity is noted when the WDXRF spectra of the Hg-containing samples, prior to and after washing with distilled water, are compared (see Figure 8).

The group is attempting to develop methods for utilizing the intensities of the "marker" peaks as the basis for making the matrix absorption effects to the intensities of the analyte peaks, so that the latter may be used to provide realistic measurements of the analytes sequestered onto the WOMBAT TDP.

CONCLUSIONS. The WOMBAT TDP sequesters several metal ions from aqueous solutions. Of these ion, both copper(II) and mercury(II) may be removed from the TDP by washing with distilled water.

REFERENCES.

Wertz, D. L. et al., ***Am. Chem. Soc., Div. Fuel Chem.*,1999**, 44, 998; **1998**, 43, 796; **1998**, 43, 349; **1997**, 42, 741; **1995**, 41, 879; **1994**, 39, 815.

Wertz, D. L., Smithhart, C. B., and Wertz, S. L., ***Adv. X-Ray Anal*, 1990**, 33, 475.

Wertz, D. L., DuBose, S. B., and Trahan, A. D., ***Adv. X-Ray Anal.*, 2000**, submitted.

Jenkins, R., "X-Ray Fluorescence Spectrometry", Wiley-Interscience, NY, 1999.

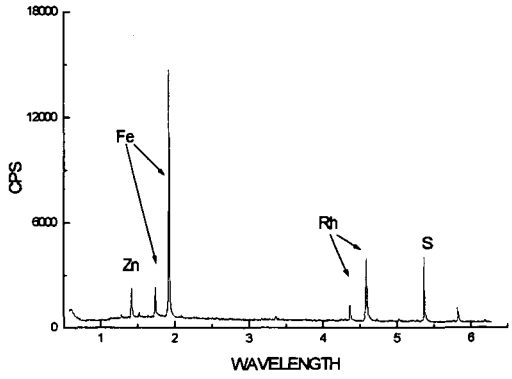

Figure 1. WDXRF spectrum of the WOMBAT TDP.

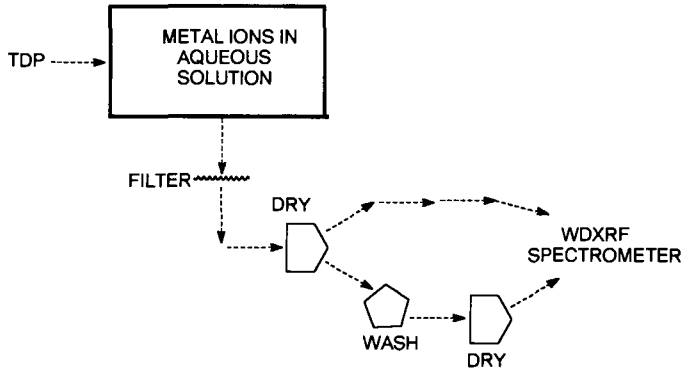

Figure 2. Schematic of the sequestering-washing experiments using WOMBAT TDP.

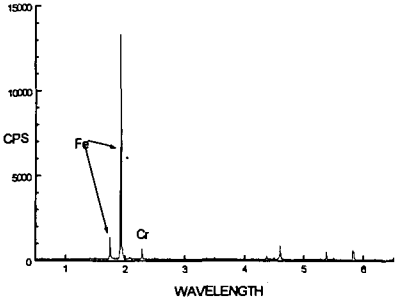

Figure 3. WDXRF spectrum of Cr-TDP.

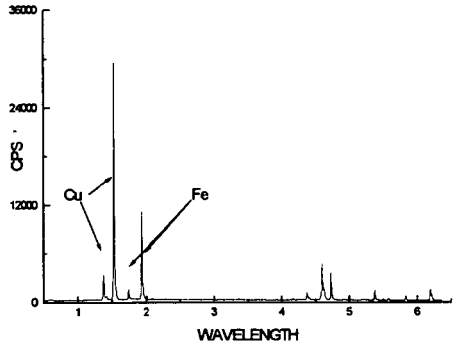

Figure 4. WDXRF spectrum of Cu-TDP.

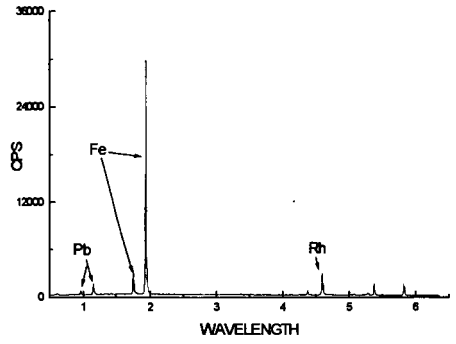

Figure 5. WDXRF spectrum of Pb-TDP.

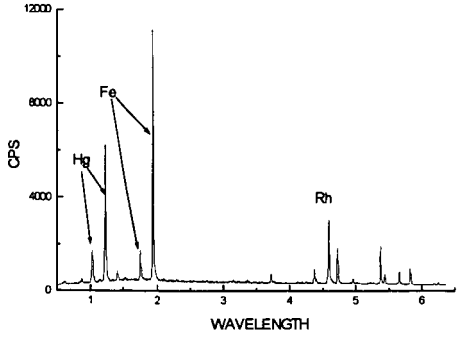

Figure 6. WDXRF spectrum of the Hg-TDP.

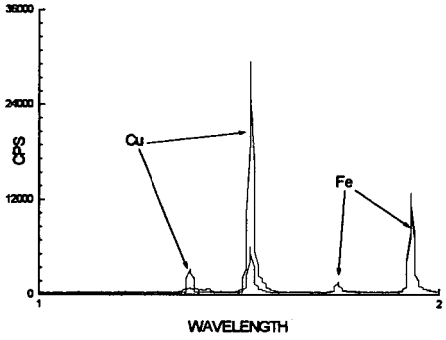

Figure 7. Comparison of the WDXRF spectra of Cu-TDP prior to and after washing with water.

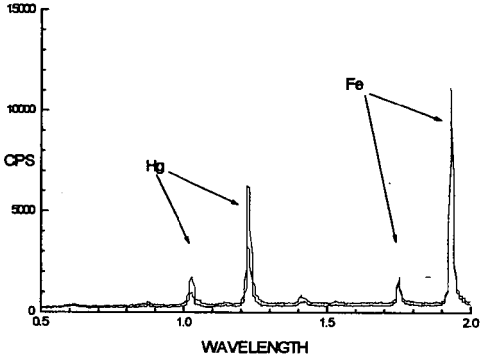

Figure 8. Comparison of the WDXRF spectra of Hg-TDP prior to and after washing with water.